Calculation of the photothermal conversion efficiency

The photothermal conversion efficiency (μ) of the BNNG@PPEG was determined according to the method reported .The detailed calculation was given as follows: In the present study[1]. The total energy balance during the photothermal heating process may be expressed as

$$\sum_{t} m_t C_{p,t}\frac{dT}{dt} = Q_{laser} - Q_{sur} \qquad 1$$

where, m (g) and Cp (J/ (g•°C)) are the mass and heat capacity of water at constant pressure, respectively, T (°C) is the temperature of the solution at time t, Q_{laser} (mW) is the energy coming from laser irradiation, and Q_{Surr} (mW) is the energy dissipated from the surface of the system to the surrounding medium. For Q_{laser} there are 2 contributions. The first term is the energy inputted by the BNNG@PPEG into the dispersion, Q_{NS}, as given by equation 2,

$$Q_{Ns} = I(1 - 10^{A_\lambda}) \qquad 2$$

where I (mW/cm^2, 1000 mW/cm^2) is the laser power, Aλ is the absorbance of BNNG@PPEG at the wavelength of 808 nm (Figure S7), and η is the efficiency of converting absorbed light energy into thermal energy.

On the other hand, the absorbance by the walls of the cuvette and the solution, Q_{Dis} (mW). The temperature is independently measured to be 29.89 mW using withoutBNNG@PPEG pure water. Thus, we get

$$Q_{laser=}Q_{NS} + Q_{Dis=}I(1 - 10^{A_\lambda})\text{+3.5mw} \qquad 3$$

Furthermore, the energy dissipation is typically expanded as a Taylor series of the HT. Within our

experimentally, the first term is used, yielding

$$Q_{sur} = hS\Delta T = hS(T - T_{sur}) \qquad 4$$

Where h (mW/(m^2•°C)) is heat transfer coefficient, S (m^2) is the surface area of the container, and T_{Surr} is ambient temperature of the surroundings. When the heat input is equal to heat output, the system reaches the steady state, and the temperature rises to a maximum, TMax (°C). In this case, the left side of Equation 6 becomes zero, we then obtain

$$Q_{laser} = Q_{sur} \qquad 5$$

Combining Equation 5 it follows that η is given by

$$\eta = \frac{hS(T_{max} - T_{sur}) - Q_{Dis}}{I(1 - 10^{A_{808}})} \qquad 6$$

In order to obtain the hS, we here introduce θ using the maximum temperature of the system, T_{max}

$$\theta = \frac{T - T_{sur}}{T_{max} - T_{sur}} \qquad 7$$

and a sample system time constant τs (s)

$$\tau_s = \frac{\sum_i m_i C_{p,i}}{hS} \qquad 8$$

Substituting Equation 7 in Equation 1 we get

$$\frac{d\theta}{dt} = \frac{1}{\tau_s}\left[\frac{Q_{NS} + Q_{Dis}}{hS(T_{max} - T_{sur})} - \theta\right] \qquad 9$$

In the aqueous dispersal cooling step of BNNG@PPEG, the laser was turned off, $Q_{NS}+Q_{Dis}=0$. $Q_{NS}+Q_{Dis}=0$. Equation 9 then becomes

$$dt = -\tau_s\frac{d\theta}{\theta} \qquad 10$$

Integrating Equation 10 we get

$$t=-\tau_s\ln(\theta) \qquad 11$$

Thus, the time constant is determined to be τ_s=305.68 s by the application of linear time data from the cooling period (after 600 s) vs-Lnθ (Figure S8). After that, according to Equation 11 we infer that hS is equal to 13.91mW/°C. Substitution of 13.91 mW/°C into Equation 5, the 808 nm laser heat conversion efficiency (η) of BNNG@PPEG can be computed at 40.552% (Table S4).

The derivation details can be found in other literature.

$$\Delta T_{max}(I_0)=\frac{R_{NP}^2\,\omega}{3K_0 8\pi}\left|\frac{3\varepsilon_0}{2\varepsilon_0+\varepsilon_{NP}}\right|^2 \mathrm{Im}\,\varepsilon_{NP}\frac{8\pi\cdot I_0}{c\sqrt{\varepsilon_0}} \qquad 12$$

ε_{NP} dielectric constant has a complex number form, with ε′ (the real part) representative capacitance, ε″ (imaginary part of dielectric constant) represent the energy storage and dissipation capability[2-4].

$$\Delta T_{max} \propto \varepsilon'' \propto B_{\text{(mass content of boron in BNNG)}} \qquad 13$$

$$\varepsilon_{NP}=\varepsilon'-j\varepsilon'' \qquad 14$$

The mass content of boron in BNNG nanoparticles was found to be positively correlated with photothermal temperature from Figure 4h, and through literature we found a positive correlation between nanoparticle temperature and the imaginary part of the dielectric constant of the nanoparticles and nanoparticles. Meanwhile, BNNG boron mass content and succulence were correlated with previous literature reports.

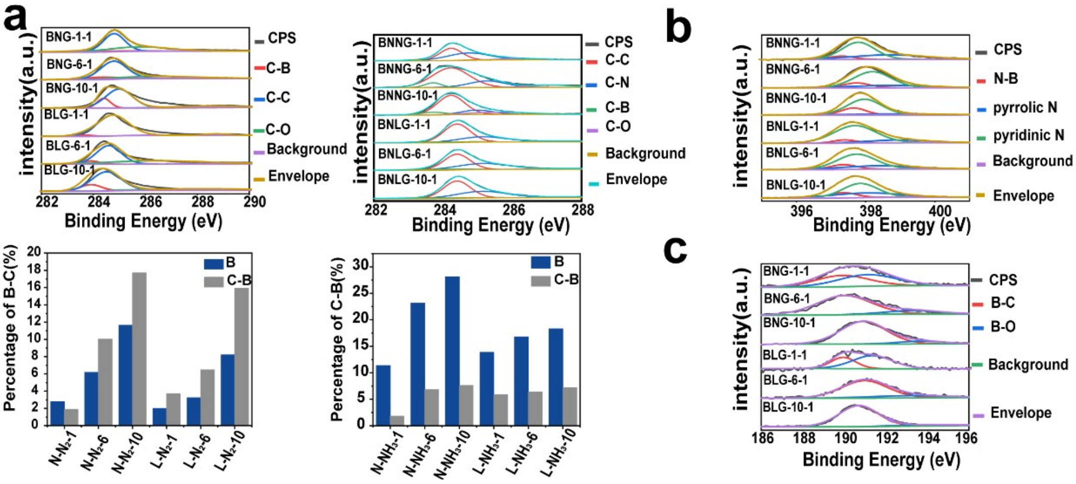

Figure S1. XPS detailed spectra of elements C, N, B, where (a), (b), (c) are the XPS detailed spectra of C, N, B 1s for BNG, BLG, BNNG and BNLG, as well as the statistics and comparison of C-B bonds and boron content.

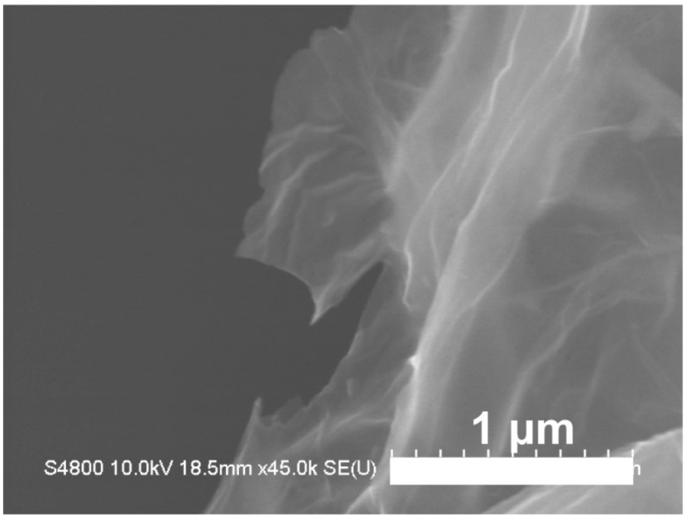

Figure S2. SEM image of BNNG.

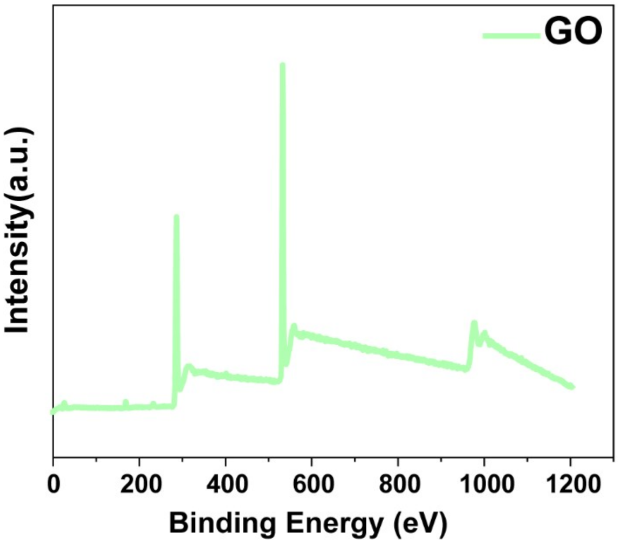

Figure S3. XPS Survey spectra of GO.

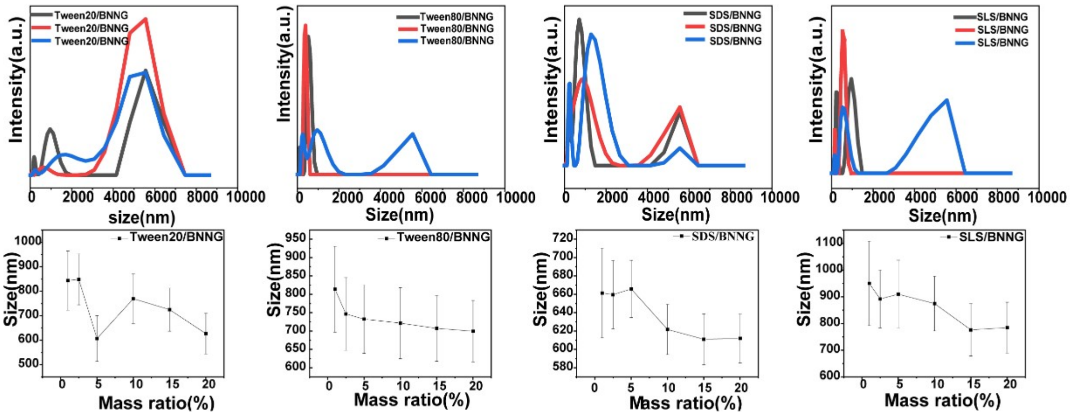

Figure S4. The water dispersibility and particle size of Boron Nitride-Graphene (BNNG) dispersions in water with different surfactants Tween80, Tween20, Sodium Dodecyl Sulfate (SDS), Sodium Lauryl Sulfate (SLS), and PEG can be measured using Dynamic Light Scattering (DLS).

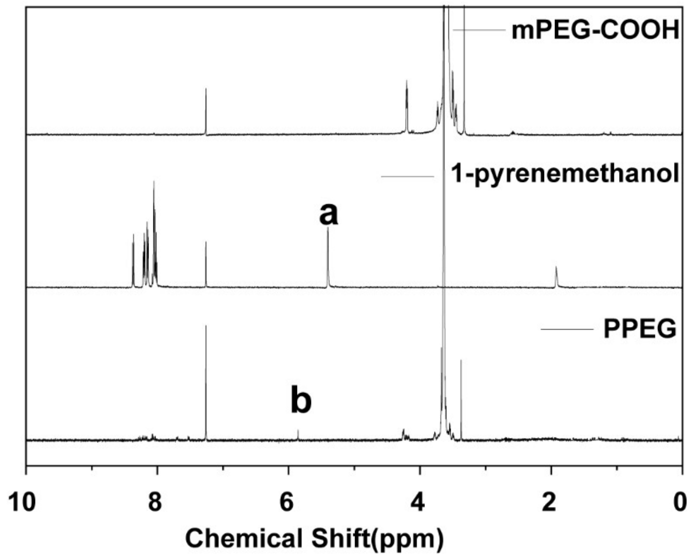

Figure S5. H NMR of mPEG-COOH, 1-pyrenemethanol and PPEG.

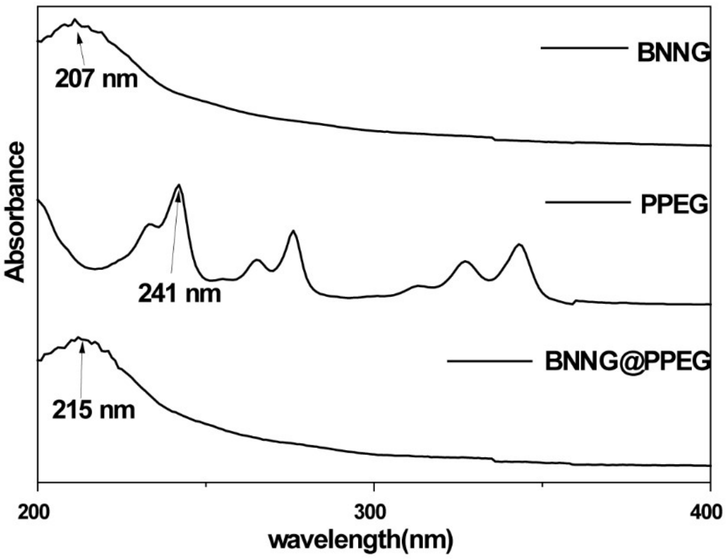

Figure S6. UV-vis absorption spectra of BNNG, PPEG, and BNNG@PPEG.

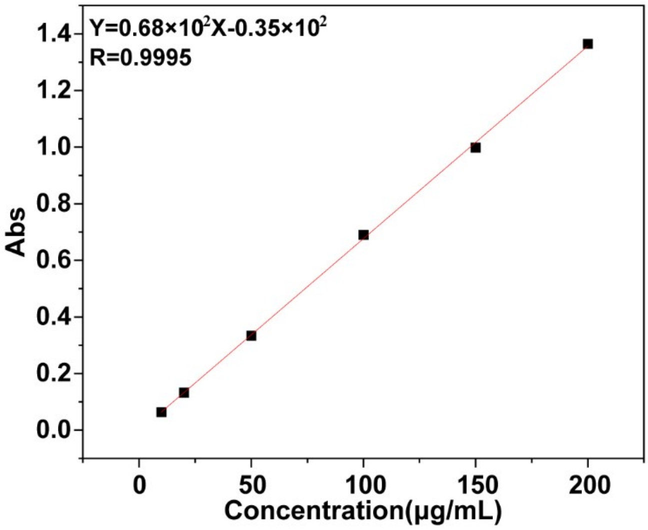

Figure S7. The concentration dependence and linear relationship of absorption spectral intensity of BNNG at 808 nm in UV-vis.

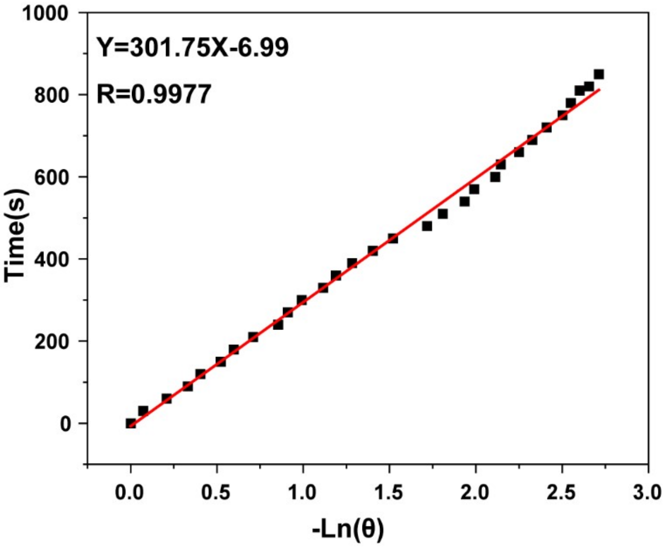

Figure S8. There is a linear correlation between the cooling time and the negative natural logarithm of the driving force temperature. Time constant (τs) for heat transfer from the system is determined to be 305.68 s.

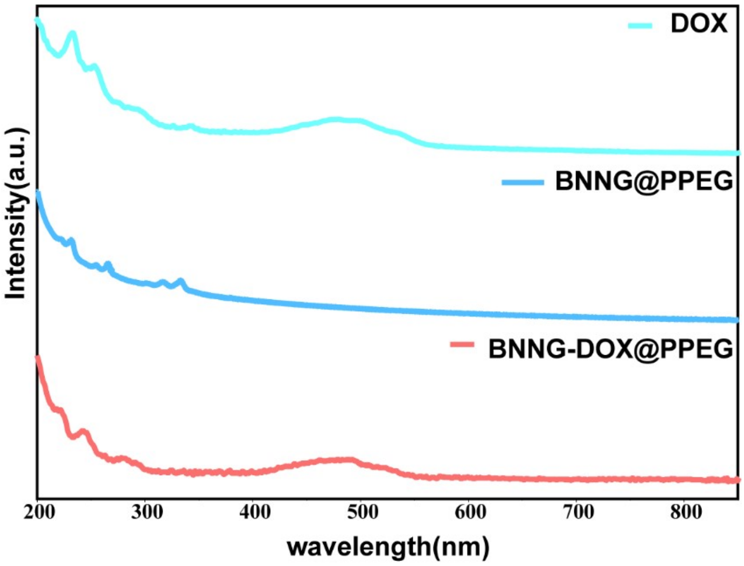

Figure S9. UV-vis absorbance spectra of DOX, BNNG and BNNG/DOX.DOXloaded on BNNG was evidenced by an additional absorption peak centered at ~500 nm.

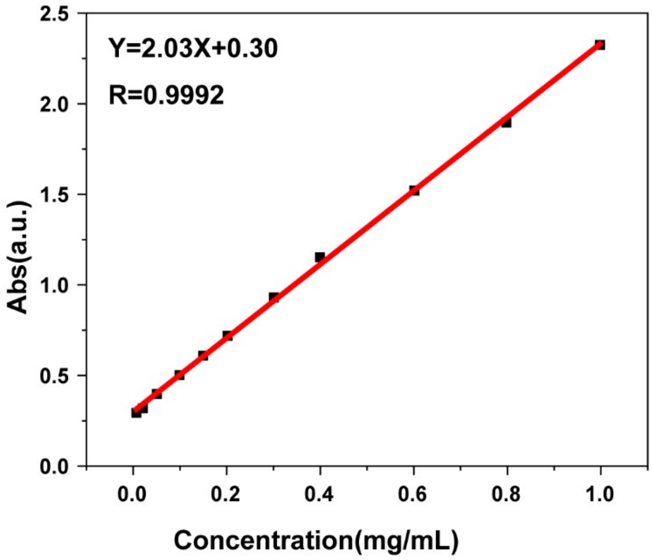

Figure S10. Plots of linear fitting extinction versus wavelength for BNNG-DOX@PPEG aqueous solution with various concentrations at 475 nm, which was used to determine the concentration of the unknown BNNG-DOX@PPEG aqueous dispersions.

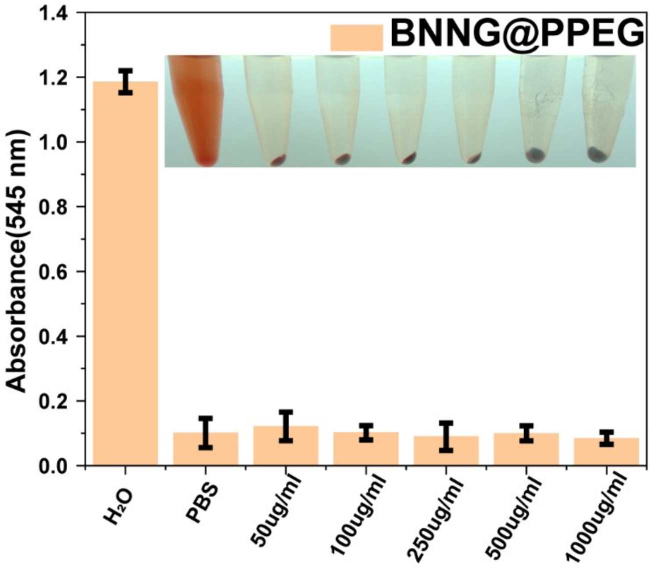

Figure S11. Hemocompatibility of different concentrations of BNNG@PPEG. Hemolysis assay. Results are presented as mean ± standard deviation (n=3).

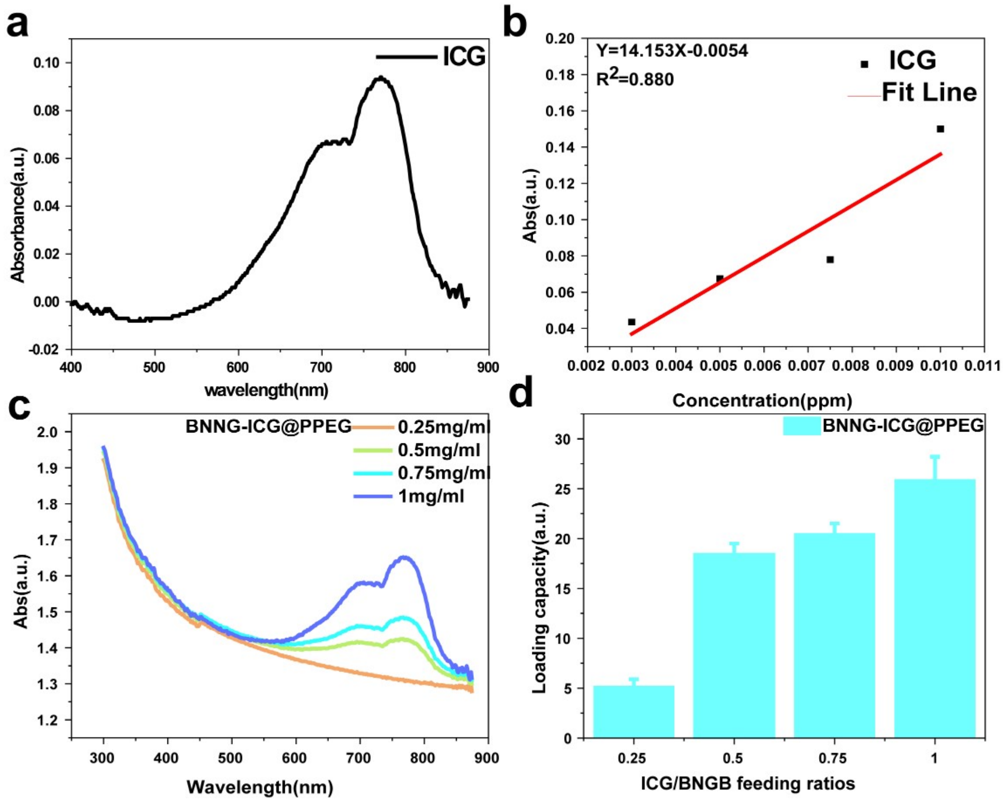

Figure S12. (a) UV-Vis absorption spectrum of ICG in aqueous solution. (b) Spectra showing the correlation of UV absorption with different concentrations of ICG. (c) UV absorption spectrum of BNNG-ICG@PPEG loaded with different concentrations of ICG. (d) Drug loading efficiency at different ICG/BNNG concentration ratios.

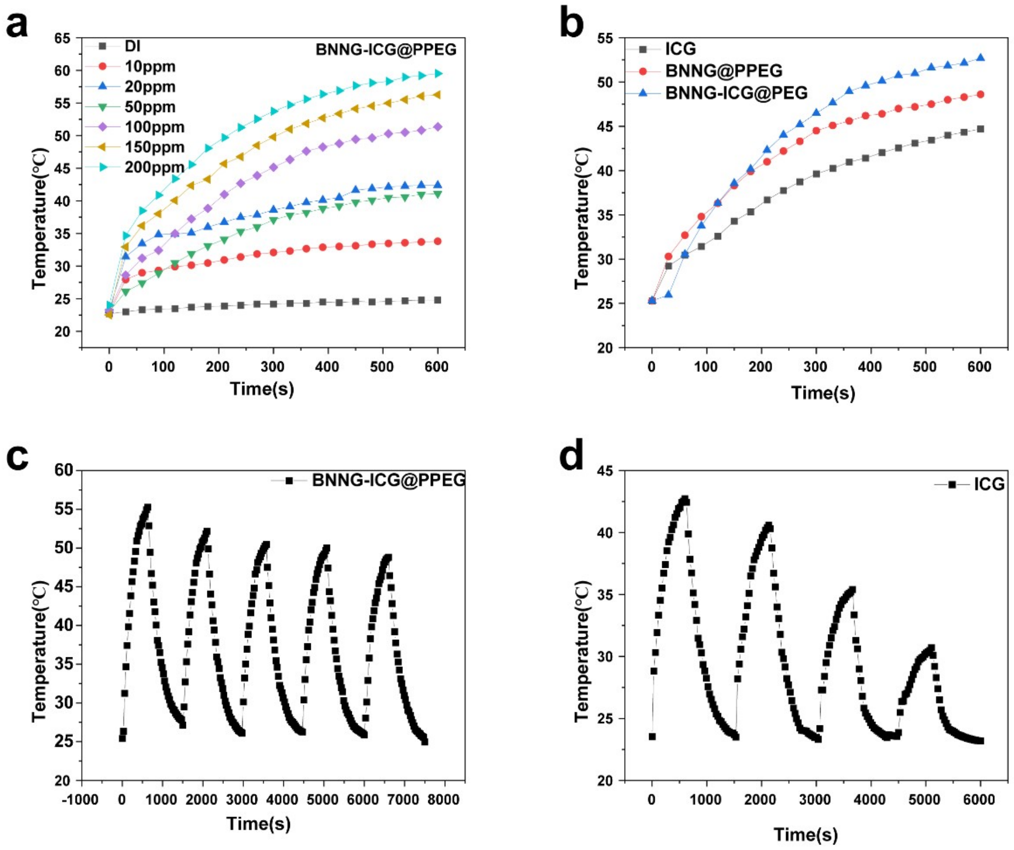

Figure S13. (a) Temperature elevation curves of BNNG-ICG@PPEG at different concentrations (ICG = 0, 10 mg/L, 20 mg/L, 50 mg/L, 100 mg/L, 150 mg/L, 200 mg/L) under near-infrared laser irradiation (808 nm, 1W, 10 min); (b) Temperature elevation curves of ICG, BNNG@PPEG, and BNNG-ICG@PPEG under near-infrared laser irradiation (808nm, 1 W/cm^2, 10 min). (c) Study on photothermal stability of BNNG-ICG@PPEG during five heating-cooling cycles. Aqueous solution of BNNG@PPEG nanosheets (100 mg/L). Each cycle includes 5 radiation and 10 min cooling stages (power density: 1.0 W/cm^2). (d) Study on photothermal stability of ICG during four heating-cooling cycles. Aqueous solution of ICG (100 mg/L). Each cycle includes one radiation and 10 minute cooling stage (power density: 1.0 W/cm^2).

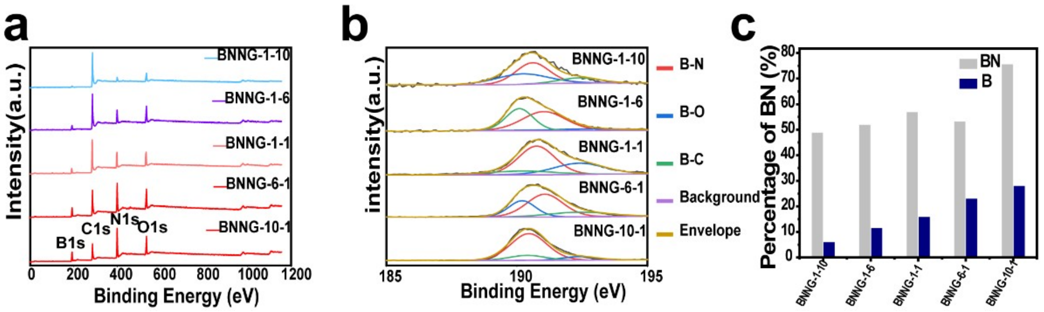

Figure S14. XPS Survey spectra of BNNG (a). where (b), (c) are the XPS detailed spectra of B1s for BNNG, as well as the statistics and comparison of B-N bonds and boron content.

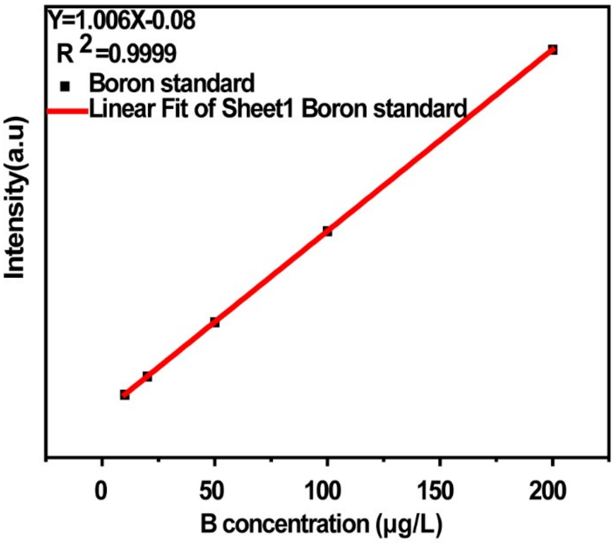

Figure S15. ICP-MS analysis spectrum of the boron standard solution curve. Assuming that there are 10^{10} cells in 1 g of tumor tissue.

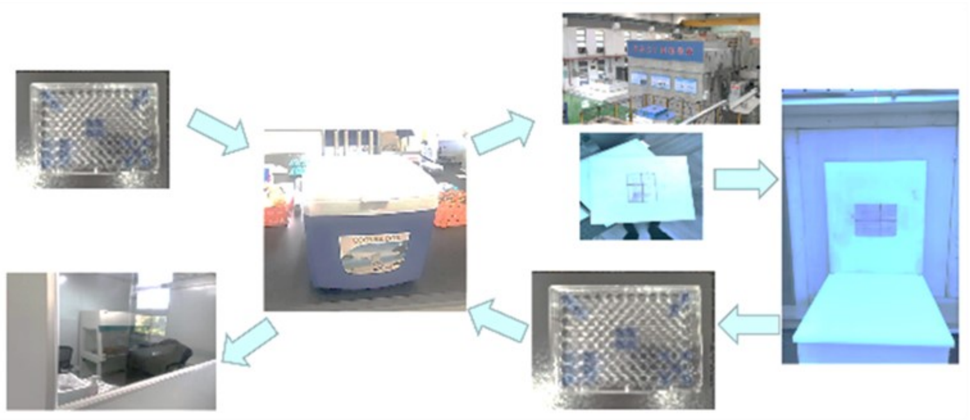

Figure S16. Schematic diagram of the BNNG-incubated cells for BNCT operation process.

As shown in Figure S17, the ^{10}B uptake capabilities of BPA and BNNG@PPEG were evaluated in vitro in the 4T1 cell line. The experimental results indicated that BNNG@PPEG exhibited higher cellular uptake efficiency than BPA at different ^{10}B concentrations. BPA targets tumor cells by specifically binding to amino acid transporters (such as LAT1) that are highly expressed in tumor cells. However, LAT1 has a bidirectional transport function, and its reverse transport mechanism can also expel BPA from tumor cells, reducing the accumulation of BPA within tumor cells[5]. In contrast, when nanoparticles approach a cell, interactions between the nanoparticles and the cell membrane generate forces from various origins. These forces promote the membrane wrapping of nanoparticles, leading to cellular uptake[6].

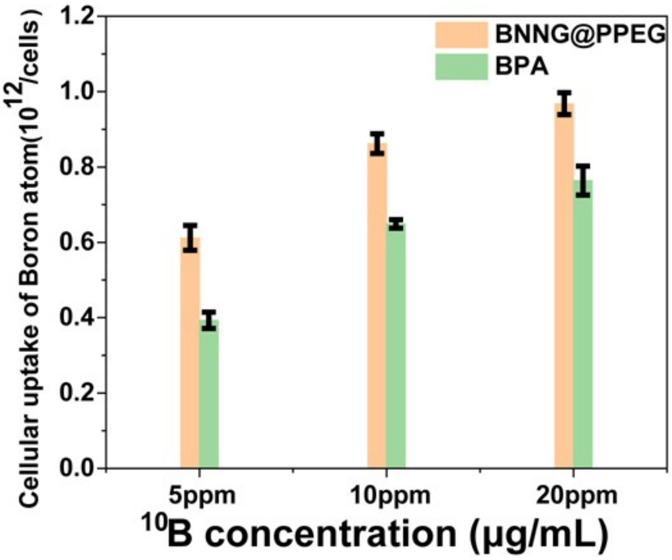

Figure S17. Cellular uptake of ^{10}B by 4T1 cells at different ^{10}B concentrations (12 h, n=4).

By comparing Figure S18, it can be confirmed that after BNNG-ICG@PPEG was undisturbed for 72 hours, the excess ICG in the supernatant was removed by centrifugation. The redissolved BNNG-ICG@PPEG in the lower precipitate showed weak UV-Vis absorption in the PBS supernatant. By comparing the ratios of UV-Vis absorption intensity at 795 nm between the PBS supernatant and BNNG-ICG@PPEG (100 μg/mL) at different treatment times (as shown in Figure 2b), we found that the intensity ratio after 72 hours was 6.12 ± 0.51%. Based on the linear correlation curve in Figure S12b, we calculated that the concentration of ICG in the PBS supernatant of BNNG-ICG@PPEG (100 μg/mL) after 72 hours was 0.001794 μg/mL. Therefore, we concluded that BNNG-ICG@PPEG has good stability in PBS, with minimal leakage of ICG.

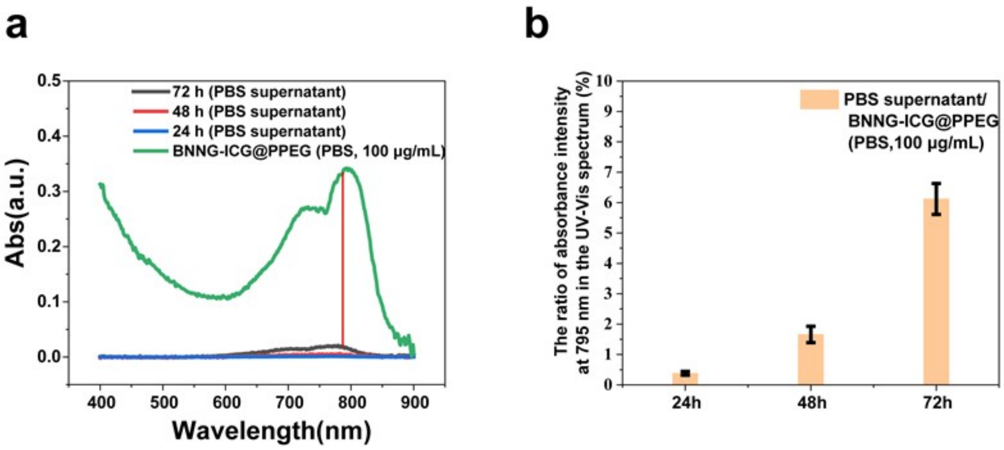

Figure S18. Leakage of BNNG-ICG@PPEG under simulated biological conditions in PBS (separating the PBS supernatant after BNNG-ICG@PPEG was left undisturbed in PBS for different durations). (a) UV-Vis absorption spectra of the PBS supernatant after different durations of undisturbed settling. (b) The ratio of the UV-Vis absorption intensity at 795 nm between the PBS supernatant and BNNG-ICG@PPEG.

Table S1. Boron-doped graphene materials from BNG to BNLG.

H_3BO_3/GO	N_2-1-1	N_2-6-1	N_2-10-1	NH_3-1-10
Nano (GO-100nm)	BNG-1-1	BNG-6-1	BNG-10-1	BNNG-1-10
Large (GO-500nm)	BLG-1-1	BLG-6-1	BLG -10-1	NA

H_3BO_3/GO	NH_3-1-6	NH_3-1-1	NH_3-6-1	NH_3-10-1
Nano (GO-100nm)	BNNG-1-6	BNNG-1-1	BNNG-6-1	BNNG-10-1

Large (GO-500nm)	NA	BNLG-1-1	BNLG-6-1	BNLG-10-1

***Note:** N_2 and NH_3, representing dinitrogen and ammonia respectively, are key reactants in the Chemical Vapor Deposition (CVD) process. A mass ratio of 1-1 signifies the proportion of boric acid to graphene oxide (GO) in the feedstock, which is essential for controlling the reaction conditions and outcomes in the CVD process.

Table S2 Doped graphene's B1s, C1s, N1s fine spectrum statistics.

Sample (Atomic ratios)	B(at%)	C(at%)	N(at%)	O(at%)
BNG-1-1	2.8	84.5	NA	12.7
BNG-6-1	6.6	83.48	NA	9.9
BNG-10-1	9.87	80.86	NA	9.36
BNNG-1-10	6.18	78.06	6.5	9.26
BNNG-1-6	11.64	64.35	12.9	11.11
BNNG-1-1	11.37	64.23	8.51	15.88
BNNG-6-1	23.16	42.71	22.56	11.58
BNNG-10-1	28.14	30.62	29.15	12.09
BLG-1-1	2.31	84.67	NA	13.02
BLG-6-1	3.69	87.07	NA	9.24
BLG-10-1	9.42	77.76	NA	12.81
BNLG-1-1	16.03	59.06	15.89	9.03
BNLG-6-1	19.45	51.73	18.96	9.86

BNLG-10-1	21.23	48.46	20.13	10.18

Table S3 ICP-MS analysis of boron mass element in differently doped graphene.

H_3BO_3/GO	BNG-1-1	BNG-6-1	BNG-10-1	BNNG-1-1	BNNG-6-1	BNNG-10-1
B at%(N)	3.47±0.2	6.75±0.52	10.25±0.36	11.45±0.85	20.53±0.952	24.97±1.14
H_3BO_3/GO	BLG-1-1	BLG-6-1	BLG-10-1	BNLG-1-1	BNLG-6-1	BNLG-10-1
B at%(L)	2.31±0.41	3.64±0.25	9.11±0.23%	14.75±0.33	18.31±0.22	19.42±0.51

Table S4 Analyze and summarize the photothermal efficiency of BNNG-1-10, BNNG-1-6, BNNG-1-1, BNNG-6-1, and BNNG-10-1.

Sample	BNNG-1-10	BNNG-1-6	BNNG-1-1	BNNG-6-1	BNNG-10-1
*T*max	40.6	42.6	44.4	45.7	48.3
*T*sur	25.5	25.5	25	25.7	25.5
K(τ s)	302.83	301.64	303.25	300.97	301.75
m(g)	1	1	1	1	1
C(J/g)	4.2	4.2	4.2	4.2	4.2
hS(mW/℃)	13.86	13.82	13.84	13.85	13.91
A_{808}	0.60	0.63	0.65	0.67	0.69
I (mW)	1000	1000	1000	1000	1000
η (%)	27.74	30.70	33.56	35.11	40.55
B/C(XPS%)	0.08	0.158	0.17765	0.54	0.91

References

[1] W. Yin, L. Yan, J. Yu, G. Tian, L. Zhou, X. Zheng, et al. High-throughput synthesis of single-layer MoS_2 nanosheets as a near-infrared photothermal-triggered drug delivery for effective cancer therapy, ACS Nano. 8 (2014) 6922-33. https://doi.org/10.1021/nn501647j

[2] M. Q. Li, M. Zhao, L. Y. Bi, Y. Q. Hu, G. Gou, J. Li, et al. Two-Dimensional Silver(I)-Dithiocarboxylate Coordination Polymer Exhibiting Strong Near-Infrared Photothermal Effect, Inorg Chem. 58(10) (2019) 6601-8. https://doi.org/10.1021/acs.inorgchem.8b02867

[3] A. O. Govorov, H. H. Richardson. Generating heat with metal nanoparticles, Nano Today. 2(1) (2007) 30-8. https://doi.org/10.1016/S1748-0132(07)70017-8

[4] O. Neumann, A. S. Urban, J. Day, S. Lal, P. Nordlander, N. J. J. A. n. Solar vapor generation enabled by nanoparticles, Nano Today. 7(1) (2013) 42-9. https://doi.org/10.1021/nn304948h

[5] NOMOTO T, INOUE Y, YAO Y, et al. Poly(vinyl alcohol) boosting therapeutic potential of p-boronophenylalanine in neutron capture therapy by modulating metabolism [J]. Sci Adv, 2020, 6(4): eaaz1722. https://www.science.org/doi/pdf/10.1126/sciadv.aaz1722

[6] ZHANG S, GAO H, BAO G J A N. Physical principles of nanoparticle cellular endocytosis [J]. 2015, 9(9): 8655-71. https://doi.org/10.1021/acsnano.5b03184